Nuclear Instruments and Methods in Physics Research A277 (1989) 23–28
North-Holland, Amsterdam

THE EAS–TOP ARRAY AT $E_0 = 10^{14}$–10^{16} eV: STABILITY AND RESOLUTIONS

M. AGLIETTA [2,3], G. BADINO [1,3], L. BERGAMASCO [1,3], C. CASTAGNOLI [2,3], A. CASTELLINA, [2,3], G. CINI [1,3], M. DARDO [1,3], B. D'ETTORRE–PIAZZOLI [2,3], W. FULGIONE [2,3], P. GALEOTTI [1,3], P. GHIA [2,3], G. MANNOCCHI [2,3], C. MORELLO [2,3], G. NAVARRA [1,3], L. PERIALE [2,3], P. PICCHI [1,3] O. SAAVEDRA [1,3], G. TRINCHERO [2,3], P. VALLANIA [2,3], and S. VERNETTO [2,3]

[1] *Istituto di Fisica Generale dell'Università, Torino, Italy*
[2] *Istituto di Cosmo–Geofisica del CNR, Torino, Italy*
[3] *Istituto Nazionale di Fisica Nucleare, Torino, Italy*

The characteristics of the EAS–TOP extensive air shower array as a detector of very high energy cosmic rays ($E_o \geq 10^{14}$ eV) for astrophysical studies are discussed. The array is located on top of the underground Gran Sasso Laboratory in central Italy; a subarray (11 modules of the em detector) has been operating since the end of 1987. From such data the stability of the detector, the timing resolution, the accuracies in the determination of the arrival directions ($\delta\theta = 1.2°$ at $E_0 \sim 200$ TeV in the present configuration) and in the reconstruction of the lateral electron distribution and of the shower size are derived.

1. Introduction

The study of the sources, of the acceleration processes and of the propagation of high-energy cosmic rays is of particular interest in astrophysics, although much experimental information is still required. While at low energies direct measurements are possible through detectors operating on balloons or satellites, at energies $E_0 \geq 10^{14}$ eV, due to the low intensities (≤ 1 [m^2 s sr]$^{-1}$) and to the large amount of material necessary for absorbing their cascades, primary cosmic rays can only be studied by exploiting the products of their interaction with the atmosphere, i.e. extensive air showers (EAS).

The quantities to be measured are:

(a) the energy spectrum, characterized by power laws over many decades and by a steepening ($\Delta\gamma \simeq -0.4$) at primary energy $E_0 \simeq 3 \times 10^{15}$ eV [1];
(b) the composition, well known at energies $E_0 \leq 10^{13}$ eV; its possible changes around the quoted "knee" of the primary spectrum could be particularly significant, being related to source or propagation properties [1];
(c) the anisotropies, well established at primary energies $E_0 = 10^{13}$–10^{14} eV (amplitude and phase of first and second harmonics: $A_1 \simeq 5 \times 10^{-4}$, $\Phi_1 \simeq 1.2$ h lst (lst = local sidereal time), $A_2 \simeq 2 \times 10^{-4}$, $\Phi_2 \simeq 6$ h lst [2]), but still uncertain at higher energies, due to statistical problems;
(d) possible γ-ray sources, that could be cosmic ray sources (a new branch of astronomy, which is developing since a few years [3–5]).

Moreover, for many years cosmic rays have been exploited as sources of high-energy particles for performing high-energy interaction experiments. This is not the case anymore, due to the high energy and high luminosity of up-to-date accelerators, except for the study of nucleus–nucleus interactions, i.e. the search for possible formation and decay of a quark–gluon plasma [6] (following the low-energy data, a fraction $f_1 \geq 10\%$ of primaries have $Z \geq 20$, and $f_2 \geq 23\%$ have $Z \geq 10$, for fixed total energy threshold).

For some of such studies, such as primary composition, γ-ray astronomy (i.e. development of selection criteria for γ primaries) and high-energy interactions, multiparameter experiments are necessary. The EAS components to be measured are: the electromagnetic one (for obtaining the shower size N_e and the shower age s from the shape of the lateral electron distribution), the low- ($E_\mu \sim$ GeV) and high-energy ($E_\mu \sim$ TeV) muons, hadrons, optical and radio emissions. For other measurements, i.e. of spectra, anisotropies and γ-ray astronomy, the stability and continuity of operation are major requirements.

Moreover, the minimum detectable flux from a point source is strongly dependent on the angular resolution: $\Phi_{\min} \propto \delta\theta/\sqrt{N_{cr}}$, where N_{cr} is the total counting rate of the array. Since the arrival angles are obtained by the time-of-flight technique, the timing resolution, its absolute calibration and the stability of TACs are essential. Besides the instrumental resolution (δt_i), the timing accuracy δt is determined by the thickness of the shower disc ($\delta t^2 = \delta t_i^2 + \delta t_{EAS}^2$) that depends on different EAS parameters (shower size, age, detection dis-

0168-9002/89/$03.50

tance from axis) and therefore must be studied for each individual array.

In this article we will discuss some characteristics (stability and resolution) of the detector of the em component of the EAS–TOP array as derived from the 11 modules in operation since the end of 1987. The performance of the detector in the various fields of operation and some technical characteristics have already been published [7–10].

2. The array

The array is located above the Gran Sasso underground laboratory (UL; latitude 42° 27′ North, longitude 13° 34′ East), 27.5° with respect to its vertical, in correspondence to the minimum thickness of rock, at the altitude of 2000 m above sea level (a.s.l.) (the altitude of the UL is 1000 m a.s.l.). The full array (fig. 1) consists of:

EMD: the detector of the em component, built of 29 modules of scintillators 10 m^2 each, separated by 17 m near the center, and by 80 m at the edges of the field (total enclosed area $A_e \simeq 10^5$ m^2);

MHD: a central 200 m^2 detector of hadrons ($E_h \geq 50$ GeV) and muons ($E_\mu \geq 2$ GeV), a calorimeter of iron and lead, seen by 8 layers of plastic tubes, operating (a) in limited streamer mode for μ-tracking, and (b) in quasi-proportional mode with controlled gain for hadron calorimetry. This detector will be covered by a layer of scintillators for the study of low-energy showers and of the EAS core structure.

In a next step the array will be implemented by means of atmospheric Cherenkov light, radio EAS detectors (already under check) and distributed low-energy muon chambers.

The apparatus will operate as an independent EAS detector and in coincidence with the underground muon detectors. The muon energy threshold corresponding to the thickness of rock between EAS–TOP and the UL is $E_\mu^{th} = 1.7$–2.0 TeV.

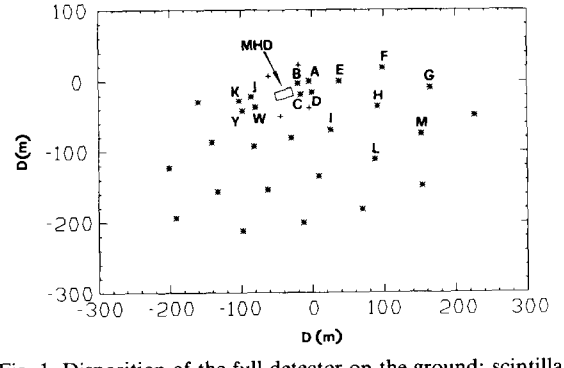

Fig. 1. Disposition of the full detector on the ground; scintillator modules: 10 m^2 (*) and 2.5 m^2 (+).

Table 1
Characteristics of the individual scintillator detectors and their measured response to single particles

Scint.	Thickness [cm]	PM distance [cm]	Npe/part.	HWHM/Hmax	Time res [a] [nsec]
Liquid	20	12 [b]	350	0.27	1.6
Plastic	4	30 [c]	40	0.20	1.4

[a] For single particles.
[b] Realized by means of a plexiglas cylinder of 21 cm diameter plunged in the liquid.
[c] Inside a diffusing box.

Due to the peculiar site on the mountain, with difficult access during winter, it has been necessary to develop procedures for on-line checking, and automatisms for replacing wrong operators.

3. The electromagnetic detector

3.1. The scintillator modules

Each 10 m^2 module is split into 16 scintillators; every scintillator is seen by two XP3462B photomultipliers with a rise-time $\tau = 3$ ns, a gain $\simeq 2 \times 10^6$ at $V_{al} \simeq 1850$ V, and linearity up to 100 mA for timing (high gain: HG) and up to 200 mA for amplitude (low gain: LG) measurements. ADC scales and PM gains are adjusted to cover respectively the ranges HG: $n_p \leq 120$ particles/module and LG $100 \leq n_p \leq 10^5$ particles/module. Four modules (A, B, C, D) are filled with liquid scintillator, all others with NE102A plastic (the dimensions of the individual detectors are 80×80 cm, other characteristics are shown in table 1).

Each scintillator module is contained in a thermally insulated ($K \leq 0.3$ kcal h^{-1} m^{-2} deg^{-1}) and stabilized box; the temperature of the liquid scintillator is stabilized at better than 0.2°. The electronics of each box includes, besides low-voltage NIM supplies:

(a) 32 channel passive HV dividers:
(b) 2 passive mixers, 16 analog channels each;
(c) analog multiplexers;
(d) double-threshold discriminators for triggering and timing measurements;
(e) a microprocessor, linked by means of optical fiber to the central processor for driving the multiplexers and the HV dividers, and reading the high and low voltages, the discriminators' thresholds and the room temperature.

3.2. Data taking organization

The array is organized (see fig. 1) into two subarrays of four modules (S_4: A, B, C, D and J, K, Y, W), and 7

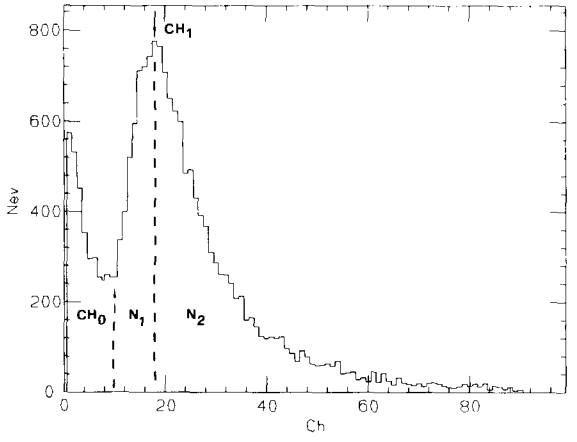

Fig. 2. Single-particle spectrum of a plastic scintillator detector, and principle of operation of amplitude calibrations from the ratio $R = N_1/N_2$.

hexagonal subarrays of 7 (or 6) modules (S_7) interconnected with each other. Triggering conditions and measurements (2 ADCs + 1 TDC per module) are performed in the central room. The subarrays operate in independent mode: any fourfold coincidence of neighbouring modules (threshold ~ 0.3 p/module) triggers the subarray. ADCs an TDCs are respectively Lecroy 2249W and 2228A (500 ps/channel). Data are taken by means of a PC IBM/AT and a microVAX connected by means of a radiotelephone link to the INFN national network. At present all data are transmitted (~ 4 kbaud) for analysis and backup to the VAX 8600 to the Torino INFN section.

3.3. Detector checking

The amplitude response of individual scintillators is adjusted and checked by using the single-particle spectra. The ratio $R = N_1/N_2$ between the number of counts above the predetermined channel (CH_1) corresponding to the peak of the single-particle distribution (N_2) and the number of counts (N_1) between the channel corresponding to the minimum of such a distribution (CH_0) and CH_1 is measured (see fig. 2). The relation between the detectors' gain G and the ratio R is: $\Delta G/G = -0.27\Delta R$; with a counting rate $f = 170$ s^{-1}, $\Delta G/G$ is checked at a 1% level in < 2 min of operation. The change in PM transit time as a consequence of changes in gain (i.e. in voltage supply) is $\Delta t = 3\Delta G/G$ ns, which allows changes of HV supplies for compensating changes of gain $\Delta G/G \sim 10\%$, without interfering with the time calibration (the measured variations of $\Delta G/G$ are of a few percent).

The timing response of individual scintillators is adjusted by comparing the time delay between the different scintillators of a module with a reference one. Since the minumum frequency of twofold coincidences in a module is 0.75 s^{-1} and the corresponding width of the delay distrubution is 7.5 ns, a maximum time measurement of ~ 5 min is required for a ≤ 0.5 ns accuracy in the calibration. A system based on a pulsed nitrogen laser ($\lambda = 337$ nm, $f \leq 50$ Hz, $P = 4$ mJ) [11] has been checked to perform on-line tests of timing and amplitude stability. The light beam emerging from the laser feeds into an optical integrating sphere to be distributed uniformly into 200 optical quartz fibers 350 m long. After being splitted inside the module to reach all PMs, such light pulses can provide a continuous time calibration of all individual channels at $\delta t < 0.5$ ns.

4. EAS results

11 modules have been running since the end of 1987: A, B, C, D (S_4: positioned at the corners of a square, 10 m^2 each), and E, F, G, H, I, L, M (S_7: positioned at the center and around a circle, 2.5 m^2 of scintillator each); all scintillators are now equipped with a single HG PM. The triggering condition is homogeneous with the final one (see section 3.2). Henceforth three classes of events will be analyzed: S_4 (fourfold coincidences of A, B, C, D), $S_{7/7}$ (sevenfold coincidences of S_7) and $S_{4/7}$ (fourfold coincidence of nearby detectors of S_7). They correspond to slightly different primary energies (see table 2).

Table 2
Some measured parameters of the three triggering conditions. The mode of the energy distribution is calculated for em cascades and the power index of the cosmic ray proton spectrum is $\gamma = 2.75$.

Trigger	Rate [s^{-1}]	Barometric coeffient [%/mb]	Temperature coefficient [%/deg]	Exp.s.d./ stat.s.d. [a]	Angular res. [b] [deg]	Emode [TeV]
4	5.3	-0.71 ± 0.01	0.1 ± 0.05	1.12	4.2	30
4/7	1.1	-0.73 ± 0.02	0.24 ± 0.08	1.01	2	100
7/7	0.11	-0.79 ± 0.07	-0.03 ± 0.02	1.07	1.2	200
7/7	–	–	–	–	0.6	1000

[a] s.d. = standard deviations.
[b] At the threshold of $n_p^{th} \approx 0.3$ particles/module.

4.1. Stability

The counting rates are correlated to the atmospheric pressure and outside air temperature; the regression coefficients are shown in table 2. The regression coefficient with atmospheric pressure agrees for the three classes of events, and with the expectations [12], while the regression coefficients with the outside temperature are scantly significant.

After correcting the counting rates for the variations of the atmospheric pressure, the stability of the detectors is checked by comparing the dispersion of the number of counts in a fixed time interval ($\Delta t = 90$ s, this choice being due only to data taking reasons) with the Poisson ones. The ratio $R = \sigma_{exp}/\sigma_p$ is also shown in table 2: it is seen that the maximum nonstatistical fluctuations are much smaller than the statistical ones (from 10 to 50%).

4.2. Timing and angular resolution

The timing resolution is measured with different methods for different subarrays (some principles of operation of EAS arrays for astrophysical purposes are discussed in ref. [13]). For S_4, with square geometry, the accuracy in timing (σ_d) is obtained from the difference of the times of flight measured for individual showers on equal paralled sides ($\Delta = (T_A - T_B) - (T_D - T_C)$, see fig. 1). The error in the measurements of a single delay is $\sigma_d = \sigma_\Delta/\sqrt{2}$. The error in the arrival direction at the zenith is $\sigma_\theta = c\ \sigma_d/D$, where D is the distance between the detectors. The timing resolution depends on the number of detected particles. Example distributions of Δ for different thresholds in the number of particles per module are shown in fig. 3. The data are summarized in fig. 4 where they are compared with the relationship expected by assuming a dependence of the timing accuracy on the number of particles: $\sigma_d \sim 1/\sqrt{n_p}$.

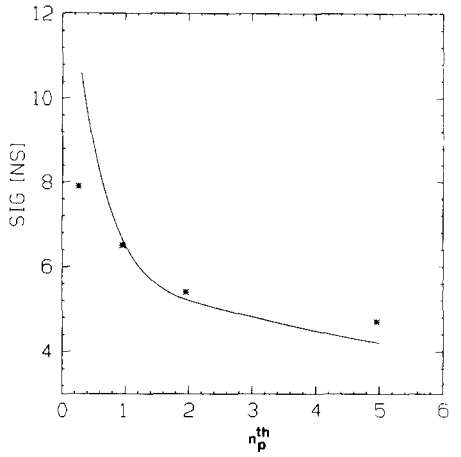

Fig. 4. Relationship between the width (s.d.) of the distributions of the "parallel delays" and the threshold number of particles/module (*); the full line shows the expected relationship, calculated by assuming a dependence of the timing accuracy: $\sigma_d \propto 1/\sqrt{n_e}$.

The angular resolution for the sevenfold coincidence $S_{7/7}$ is obtained by dividing the array into two subarrays (E, G, H, L and F, H, I, M,) and by comparing the two arrival directions. The integral distribution of such a difference, for events analyzed by fitting the shower disc with a plane, (at a threshold of 0.3 particles/module, zenith angle $\theta < 30°$) is shown in fig. 5 (curve $S_{7/7}$, *), compared with the distributions obtained by assuming Gaussian shapes of fluctuations

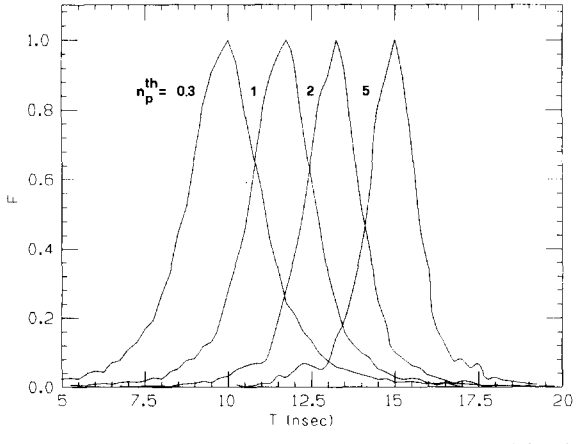

Fig. 3. Distributions of the differences of times of flight Δ measured on equal parallel sides of a square ("parallel delays"), for different thresholds in the number of particles/module. The curves are arbitrarily shifted on the horizontal axis.

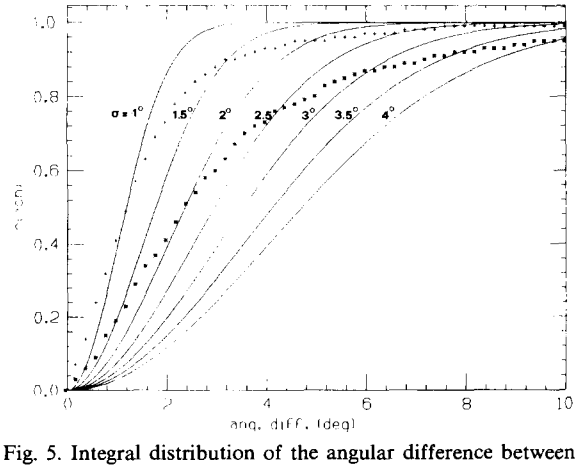

Fig. 5. Integral distribution of the angular difference between the arrival directions measured by two subarrays of the 7-detectors circle: * denotes $S_{7/7}$ and + $S'_{7/7}$. The full lines show the expectations obtained by assuming Gaussian error distributions of different standard deviations.

with different values of s.d. (= standard deviations). We see that a single Gaussian does not fit the experimental distribution; 70% of the data are enclosed inside an error box with $\sigma_{\Delta\psi} \leq 2.4°$. From statistics, when all seven detectors are used, the error in the arrival time is $\sigma_\psi = \sigma_{\Delta\psi}/2 = 1.2°$, and for $S_{4/7}$ it is $\sigma_{4/7} = \sqrt{3}\,\sigma_{7/7}$ ($\sqrt{2}$ from statistics and $\sqrt{1.5}$ from geometry). Unlike the estimates for the square configuration, this includes the possible systematic errors (i.e. the indetermination in the vertical direction).

The EAS temporal structure is characterized by a curved disc whose thickness is increasing with core distance [14–20].

After fitting the times of flight between the detectors, the thickness of the shower disc is obtained from the distribution of the distances between the experimental delays and the reconstructed curved front of the shower. Such a distribution is shown in fig. 6; its width is $\Delta s = 1.5$ m; the point near the shower axis is not included and therefore the measurement refers to core distances between 40 and 120 m at an average particle density $n_e = 6$ particles/module. An empirical fit [18] to the existing data on the thickness of the shower disc gives, in the quoted range of core distances, $\Delta z = 2$–6.8 m. This, when converted to the 6-particle level, gives $\Delta z/\sqrt{n_e} = 1$–3.5 m. This is in agreement with the experimental value Δs, thus showing that the main contribution to the fluctuations in time measurements is due to the thickness of the shower disc, while the instrumental resolution is negligible.

For sevenfold coincidences in which the core position can be determined, ($S'_{7/7}$ see section 4.3) the arrival direction is obtainable by taking into account the described EAS temporal structure, i.e. by introducing the average delay of particles and thickness of the shower disc as a function of core distance $r(d[m] = 0.016r[m]/\sqrt{n_p}$; $\sigma_{d[m]} = 0.001r^{1.25}/n_p^{0.25}$, where n_p = number of detected particles). For such events we obtain the curve $S'_{7/7}$ shown in fig. 5 (+), corresponding to a width $\sigma_{\Delta\psi} \leq 1.2°$, and therefore $\sigma'_{7/7} = 0.6°$.

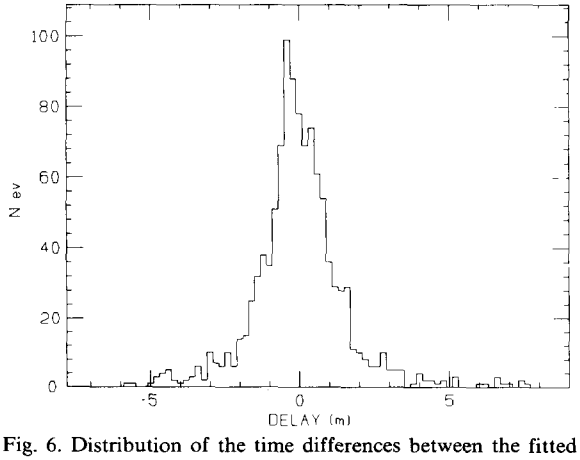

Fig. 6. Distribution of the time differences between the fitted curved front of the shower and the individual measured arrival times.

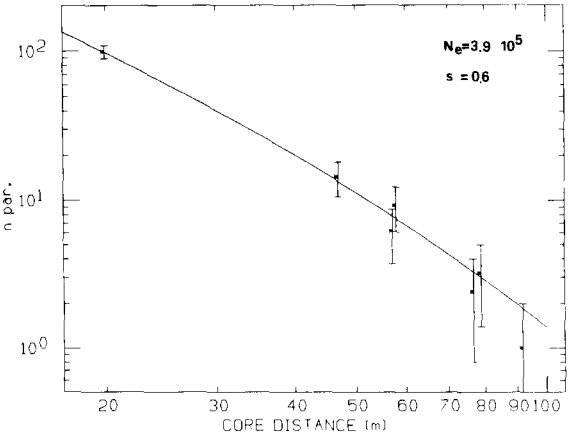

Fig. 7. Example of measured particle densities and of the reconstructed lateral distribution function of an atmospheric shower.

We want to remark that in the search for a point source:

(a) for a Gaussian distribution of fluctuations $f(\theta)$, the optimum signal-to-noise ratio ($S/\sqrt{B}$) is obtained for an opening angle $\alpha \simeq 1.6\sigma_\theta$ for which the efficiency of detecting events from the point source is $\epsilon = 70\%$;

(b) when converting the angles to the celestial coordinate system α, δ, due to the length of the minor parallel circle, $\sigma_\alpha = \sigma_\theta/\cos\delta$

4.3. Measurement of the lateral distribution and shower size

The core position, lateral distribution function and total number of shower particles (N_e) are reconstructed from the fit of the particle densities recorded by the different modules. As electron lateral distribution function we use the expression [21]:

$$\rho(r) \propto N_e \left(\frac{r}{r_0}\right)^{(s-2)} \left(1 + \frac{r}{r_0}\right)^{(s-4.5)},$$

where N_e is the shower size and s the shower age. In the present analysis, to be sure that the shower core position is inside the external circle of detectors, we will use only the events for which the higher particle density ($n_p > 20$) is recorded by the central module of S_7. An example of reconstructed lateral distribution functions is shown in fig. 7. The χ^2 fit is performed by assuming Poissonian fluctuations + 10% instrumental uncertainties in particle counting. For primary protons the mean conversion from shower size to primary energy is $E_0 \simeq 5$ GeV/ particle at $N_e \simeq 10^5$. By analyzing simulated EAS

with the same program and using the full EMD array, we obtain inside the whole enclosed area:

$$\sqrt{\langle \Delta r^2 \rangle} \leq 3 \text{ m}, \quad \frac{\Delta N_e}{N_e} < 20\% \text{ and } \Delta s < 0.1$$

at $E_0 = 10^{15}$ eV.

5. Conclusions

The main characteristics of extensive air shower arrays for astrophysical studies are discussed. A preliminary analysis of the EAS-TOP data collected in the first months of 1988 shows a good stability of the apparatus. The analysis of the angular resolution, of the arrival times and of the particle density measurements is coherent and follows the expectations.

References

[1] A.M. Hillas, Phys. Rep. C20 (1975) 59.
[2] V.V. Alexeenko, A.E. Chudakov, E.N. Gulieva and V.G. Sborshikov, Proc. 17th International Cosmic Ray Conference, Paris, 2 (1981) p. 146.
[3] K.E. Turver ed., Very High Energy Gamma Ray Astronomy, Proc. of the NATO Advanced Research Workshop, Durham, UK, August 11-15, 1986 (Reidel, 1987).
[4] A.A. Watson, Proc. 19th Int. Cosmic Ray Conf., La Jolla, 9 (1985) p. 111.
[5] R.J. Protheroe, Proc. 20th Int. Cosmic Ray Conf., Moscow, 8 (1987) p. 21.
[6] T.H. Burnett, S. Dake, M. Fuki, J.C. Gregory, T. Hayashi, R. Holynski, J. Iwai, W.V. Jones, A. Jurak, J.J. Lord, O. Miyamura, H. Oda, T. Ogata, T.A. Parnell, T. Saito, T. Tabuki, Y. Takahashi, T. Tominaga, B. Wilczynski, R.J. Wilkes, W. Wolter and B. Wosiek, Proc. 18th Int. Cosmic Ray Conf., Bangalore, 5 (1983) p. 218.
[7] M. Aglietta, C. Castagnoli, A. Castellina, B. D'Ettorre-Piazzoli, W. Fulgione, P. Galeotti, G. Mannocchi, C. Morello, L. Periale, G. Trinchero, P. Vallania, S. Vernetto, G. Badino, L. Bergamasco, G. Cini, M. Dardo, G. Navarra, P. Picchi and O. Saavedra, Nuovo Cimento C9 (1986) 262.
[8] M. Aglietta, C. Castagnoli, A. Castellina, B. D'Ettorre-Piazzoli, W. Fulgione, P. Galeotti, G. Mannocchi, C. Morello, L. Periale, G. Trinchero, P. Vallania, S. Vernetto, G. Badino, L. Bergamasco, G. Cini, M. Dardo, G. Navarra, P. Picchi and O. Saavedra, in: Very High Energy Gamma Ray Astronomy, ed. K.E. Turver (Reidel, 1987) p. 265.
[9] M. Aglietta, C. Castagnoli, A. Castellina, B. D'Ettorre-Piazzoli, W. Fulgione, P. Galeotti, G. Mannocchi, C. Morello, L. Periale, G. Trinchero, P. Vallania, S. Vernetto, G. Badino, L. Bergamasco, G. Cini, M. Dardo, G. Navarra, P. Picchi and O. Saavedra, Proc. 20th Int. Cosmic Ray Conf., Moscow, 2 (1987) p. 454.
[10] M. Aglietta, C. Castagnoli, A. Castellina, B. D'Ettorre-Piazzoli, W. Fulgione, P. Galeotti, G. Mannocchi, C. Morello, L. Periale, G. Trinchero, P. Vallania, S. Vernetto, G. Badino, L. Bergamasco, G. Cini, M. Dardo, G. Navarra, P. Picchi and O. Saavedra, Proc. 2nd Int. Symp. on Underground Physics UP-87, Baksan, USSR, p. 194.
[11] M.J. Corden, J.D. Dowell, M.J. Edwards, N.N. Ellis, J. Gavrey, D. Grant, R.J. Homer, I.R. Kenyon, T.J. McMahon, G. Schanz, K.C.T.O. Sumorok, P.M. Watkins, J.A. Wilson, A. Bezaguet, G. Gallay, G. Barnes, T.J.V. Bowcock, E. Eisenhandler, W.R. Gibson, A.K. Honma, P.I.P. Kalmus, R.K. Keeler, T.W. Pritchard, G.A.P. Salvi, G. Thompson, G.T.J. Arnison, A. Astbury, A.R. Cash, G.H. Grayer, W.J. Haynes, D.L. Hill, D.R. Moore, A.K. Nandi, M.D. Percival, J.H.C. Roberts, W.G. Scott, T.P. Shah, R.J. Stanhope and D.E.A. White, Nucl. Instr. and Meth. A238 (1985) 273.
[12] S. Sakakibara, K. Fujimoto, Z. Fujii, H. Ueno, I. Kondo and K. Nagashima, Proc. Int Cosmic Ray Symp. on High Energy Cosmic Ray Modulation, Tokyo, 1976, p. 162.
[13] C. Morello and G. Navarra, Nucl. Instr. and Meth. 187 (1981) 533.
[14] G. Bosia and G. Navarra, Nuovo Cimento B62 (1969) 301.
[15] A.M. Hillas, Very High Energy Gamma Ray Astronomy, ed. K.E. Turver, (Reidel, 1987) p. 289.
[16] T. Nakatsuka, 19th Int. Cosmic Ray Conf. (1985).
[17] M.A. Locci, P. Picchi and G. Verri, Nuovo Cimento B50 (1967) 384.
[18] J. Linsley, J. Phys. G12 (1986) 51.
[19] C.P. Woidneck and E. Boehm, J. Phys. A8 (1975) 997.
[20] P.J.V. Eames, A. Lambert, J.C. Perret, R.J.O. Reid, N.J.T. Smith, A.A. Watson and A.A. West, Proc. 20th Int. Cosmic Ray Conf., Moscow, 2 (1987) p. 449.
[21] K. Greisen, Progr. Cosmic Ray Phys. 3 (1956) 1.